Magnetism in tetragonal manganese-rich Heusler compounds

Lukas Wollmann,[1] Stanislav Chadov,[1] Jürgen Kübler,[2] and Claudia Felser[1,*]
[1]*Max-Planck-Institut für Chemische Physik fester Stoffe, Nöthnitzer Strasse 40, D-01187 Dresden, Germany*
[2]*Institut für Festkörperphysik, Technische Universität Darmstadt, D-64289 Darmstadt, Germany*
(Received 22 June 2015; published 18 August 2015)

A comprehensive study of the total energy of manganese-rich Heusler compounds using density functional theory is presented. Starting from a large set of cubic parent systems, the response to tetragonal distortions is studied in detail. We single out the systems that remain cubic from those that most likely become tetragonal. The driving force of the tetragonal distortion and its effect on the magnetic properties, especially where they deviate from the Slater-Pauling rule, as well as the trends in the Curie temperatures, are highlighted. By means of partial densities of states, the electronic structural changes reveal the microscopic origin of the observed trends. We focus our attention on the magnetocrystalline anisotropy and find astonishingly high values for tetragonal Heusler compounds containing heavy transition metals accompanied by low magnetic moments, which indicates that these materials are promising candidates for spin-transfer-torque magnetization-switching applications.

DOI: 10.1103/PhysRevB.92.064417 PACS number(s): 75.50.Gg, 71.15.Nc, 75.10.Lp, 75.30.Gw

I. INTRODUCTION

The spintronics community demands materials with uniaxial anisotropy for spin-transfer-torque-random-access-memory applications, as well as for fundamental skyrmion-related research or in the field of magnetic shape-memory alloys [1]. Such materials are needed to improve the functionality and applicability of modern devices or device concepts within the scope of mass production or proof of practicality. Addressing this request within the class of compounds with Heusler and Heusler-like structures, the task is approached by means of relatives of familiar systems [2,3]. These relatives are the family of Mn_2-based Heusler compounds, the famous pioneering material and ancestor of which is Mn_3Ga [4,5]. The uniaxial magnetocrystalline anisotropy of Mn_3Ga has been calculated [6] and measured [7] several times on different occasions. It is thought that anisotropic materials such as these could constitute the foundation for magnetic racetrack memory as proposed by *Parkin et al.* [8]. The indispensable perpendicular magnetic anisotropy in (ultra)thin structures is best controlled by intrinsic properties rather than by shape- or strain-induced anisotropy. As a result, the perpendicular orientation of magnetization is a desired property of the material. Recently, Mn_2-based Heusler systems, Mn_2YZ, were reconsidered as promising materials. Thus, considerable research has been done on related systems. Mn_2NiGa [9,10] in particular is a well-studied material as it is directly related to Ni_2MnGa, which has been the most studied and best understood ferromagnetic shape-memory alloy since its discovery [11,12]. Mn_2NiGa, however, is a ferrimagnetic shape-memory alloy that is theoretically linked to Ni_2MnGa through a substitution series, with a transition from ferro- to ferrimagnetic ordering due to the increasing manganese content. In addition to Mn_2NiGa, other Mn_2-based Heusler alloys have been synthesized and characterized or have been theoretically treated, such as Mn_2CoGa [13–17], Mn_2FeGa [18], and Mn_3Ga [4,7]. In addition to materials in which Y is an atom from period IV (or the 3*d* series), equivalent systems with heavier constituents as Y species have been investigated. Among these were Mn_2RuGa [19] (which has been found to have more or less random occupation of sites), Mn_2RhGa [20] (cubic, disordered), Mn_2PtGa [21,22], and Mn_2PtIn [23] in the context of large exchange bias effects.

Although a detailed study of a single material is an important task that results in valuable knowledge, the inclusion of cluster knowledge into a general concept creates comprehensive insight. The same intention that guided our previous work [17] motivated us to undertake a similar approach in the current study, i.e., comprehensively studying a selected set of systems. We intend to understand the general trends governing the formation and magnetism of tetragonal materials for the aforementioned applications.

In this paper, we show how the magnetism and the atomic structure change within the $Mn_2Y^{(3d)}Ga$, $Mn_2Y^{(4d)}Ga$, and $Mn_2Y^{(5d)}Ga$ series. The trigger quantities causing the tetragonal distortion, as well as the consequences of this distortion, i.e., the magnetocrystalline anisotropy (MCA) [3], will be highlighted and placed into an appropriate context.

II. CRYSTAL STRUCTURE

Heusler alloys are nowadays informally divided into two structure types, the so-called *regular* and *inverse* types, referring to the original Heusler compound Cu_2MnAl as the reference system [24]. The materials first associated with Fritz Heusler's name were cubic phases analogous to Cu_2MnAl, with the stoichiometry X_2YZ. From then on, similar materials were thus labeled "Heusler compounds," extending the original definition of Heusler compounds to the family of Heusler materials that incorporates a variety of similar structures. These structures are derived from the original compound, with occupation of the Wyckoff positions, 8*c*, 4*b*, and 4*a*, in space group (SG) 225 through the introduction of vacancies or slight structural changes. These modifications alter the structure by breaking the inversion symmetry when going from a *regular* Heusler phase to an *inverse* or *half*-Heusler structure.

Heusler materials are generally understood to be intermetallic compounds, distinguishing them from general intermetallics that form a broad range of solid solutions,

*claudia.felser@cpfs.mpg.de

TABLE I. The structural relationship of the *regular* and *inverse* structure types for Mn_2YGa is shown, where $X = X' = Mn$ and $Z = Ga$ (Fig. 1). The chemical order is given in terms of the *Strukturberichte designation*. Only one of three possible configurations of a *half*-Heusler type ordering is listed exemplary. In contrast to *full*-Heusler compounds, *half*-Heusler compounds exhibit a void (□) at one of the Wyckoff-Positions with multiplicity four.

Heusler type	Chem. ord.	SG	4*d*	4*c*	4*b*	4*a*
Regular	$L2_1$	225	Mn	Mn	*Y*	Ga
Inverse	X_a	216	Mn	*Y*	Mn	Ga
Half	$C1_b$	216	Mn	Mn	□	Ga

with no preferred but statistical occupation of crystallographic sites. They are also set apart from other ionic or covalent compounds because Heusler systems allow the formation of substitutional series of single sites. However, they maintain the character of an ordered compound, and thus they are on the borderline between alloys and compounds. Some distinct systems exhibit a tendency to form alloys nevertheless. The general composition is given by $XX'YZ$, where the classical definition has been widened to incorporate quaternary materials within the family of Heusler compounds. In the representation of SG 216 ($F\bar{4}3m$), the structure contains four highly symmetric Wyckoff positions: 4*d* ($\frac{3}{4},\frac{3}{4},\frac{3}{4}$), 4*c* ($\frac{1}{4},\frac{1}{4},\frac{1}{4}$), 4*b* ($\frac{1}{2},\frac{1}{2},\frac{1}{2}$), and 4*a* (0,0,0). Depending on the occupation of the crystallographic positions, two ordering possibilities for ternary alloys ($X = X'$) are obtained (Table I). In this study, gallium was chosen as the *Z* element, whereas one manganese atom, *X*, occupies position 4*d*. The second manganese atom, X', and the other transition metal, *Y*, are located at 4*c* or 4*b*, respectively, depending on the formation of the *regular*- or *inverse*-type Heusler material, as shown in Table I. Other Heusler-related structures [25] are the tetragonal derivatives of the cubic parent phases, which have been widely treated in the context of magnetic shape-memory alloys. The relationship and the unit-cell transformation between cubic and tetragonal phases is depicted in Fig. 1. It is seen that a conventional cubic unit cell can be described in terms of a tetragonal lattice exhibiting a c/a ratio of $\sqrt{2}$. The cell parameters are interrelated according to $c_{tet} = c_{cub}$, $a_{tet} = a_{cub}/\sqrt{2}$. In this study, a set of Mn_2-based materials, including transition metals of periods IV, V, and VI, are considered, namely, $Mn_2Y^{(3d)}Ga$, $Mn_2Y^{(4d)}Ga$, and $Mn_2Y^{(5d)}Ga$.

III. COMPUTATIONAL DETAILS

The numerical work was done within density functional theory as implemented in the all-electron full potential linearized augmented planewave (FP-LAPW) code WIEN2K [26], employing the generalized gradient approximation in the parametrization of Perdew, Burke, and Enzerhof as the exchange-correlation functional [27]. The angular momentum truncation was set to $l_{max} = 9$, and the number of plane waves was determined by $R_{MT}K_{max} = 9$, according to the smallest muffin-tin radius R_{MT} resulting in the vector for the truncation of the plane waves K_{max}, to ensure well-converged calculations. The energy convergence criterion for the self-consistent field calculations was set to 10^{-5} Ry, whereas the charge convergence was set to 10^{-3}. All calculations where done on a $20 \times 20 \times 20$ *k* mesh. For a set of given c/a ratios, the volumes were optimized and fitted to the Birch-Murnaghan equation of state [28,29]. From these, the optimal ratio and volume were obtained, and the lattice parameters were evaluated. On the basis of the crystallographic details, magnetic properties such as the exchange coupling parameters J_{ij}, the corresponding Curie temperatures T_C, and the MCA energy were computed. The MCA energy is here evaluated as the energy difference between two orientations of the magnetization, $E_{MCA} = E_{(100)} - E_{(001)}$. The underlying total energies are calculated self-consistently using WIEN2K considering spin-orbit coupling in a second variational step with an enlarged *k* mesh of $31 \times 31 \times 31$ points, resulting in 7369 *k* points in the irreducible part of the Brillouin zone. The convergence criteria were adapted according to the problem, and thus the energy tolerance was set to $\Delta_E = 10^{-8}$, while charge convergence was set to $\Delta_c = 10^{-5}$. The Korringa-Kohn-Rostoker (KKR) Green's function method as implemented by the Munich SPR-KKR package [30] was used to compute the exchange coupling constants. The angular momentum expansion of the wave function was truncated for $l_{max} = 3$, which corresponds to *f*-wave symmetry. The energy integration was done on a complex energy mesh with 48 points along the integration path using Lloyd's formula [31] for an improved estimate of the Fermi energy. The computation of the exchange parameters is based on the

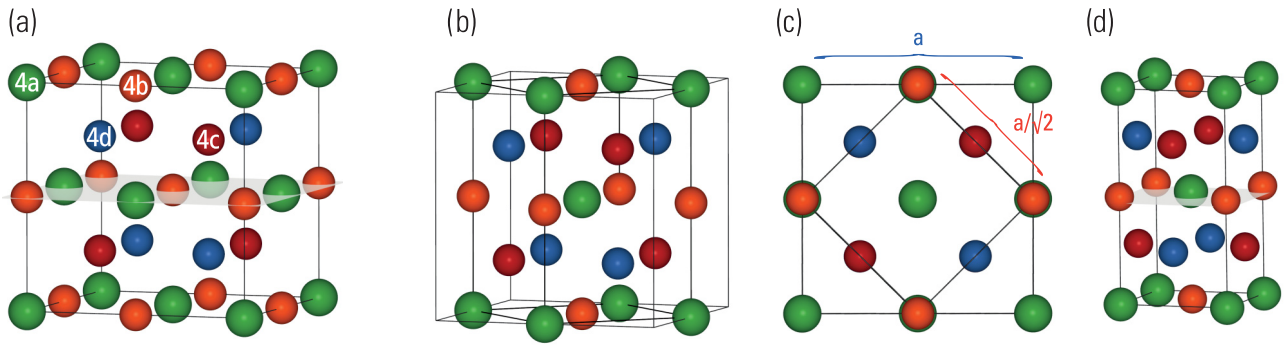

FIG. 1. (Color online) The conversion from (a) a cubic Heusler structure to (b) a tetragonal derivative phase is displayed in terms of a nondisplasive transformation for a system with the general composition of $XX'YZ$ (X, X', Y are transition metals and Z is the main-group element, marked in red, orange, blue, and green, respectively) within the fcc lattice. (c) Relationship of the lattice parameters as $a_{tet} = a_{cub}/\sqrt{2}$.

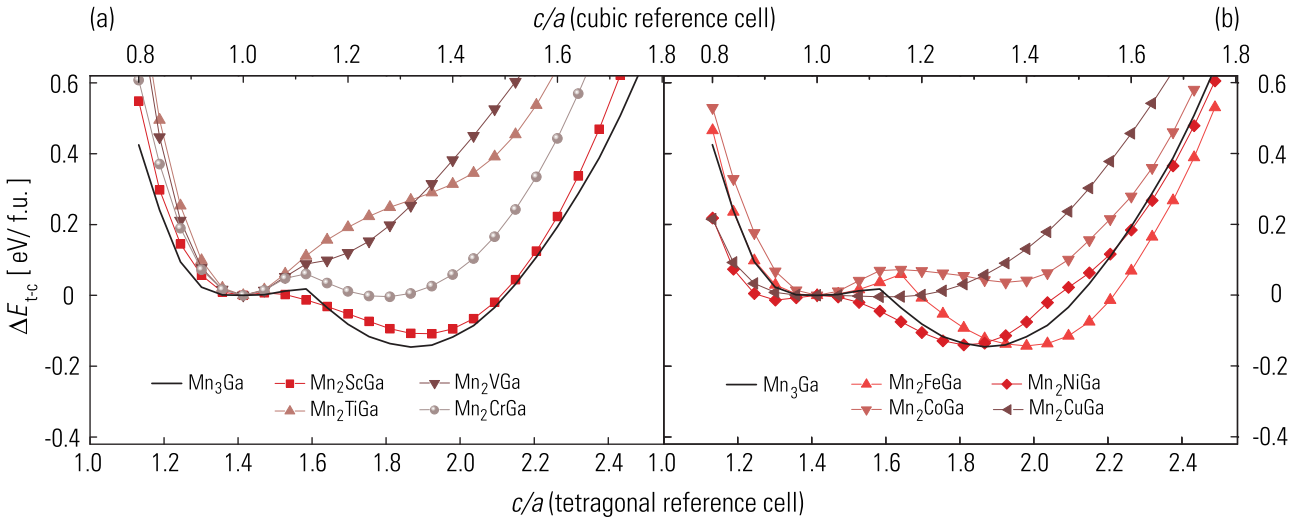

FIG. 2. (Color online) Energetic response to volume-conserving elongations and compressions of the crystal structure along the c axis for the $Mn_2Y^{(3d)}Ga$ series. (a) Systems with a valence electron count $N_V(Y) \leqslant 7$ (early transition metals) and (b) the remaining combinations of $Mn_2Y^{(3d)}Ga$ with $N_V(Y) \geqslant 7$, with so-called late transition metals.

classical Heisenberg model, which was evaluated by means of the real-space approach [32]. This provides site- and distance-dependent exchange between sites via infinitesimal rotation of the magnetic moments at a particular site in real space. To account for the distance dependence, an appropriate truncation of the cluster radius r around each atomic site was chosen. This radius was set to $3.5a$ lattice spacings to capture even small interactions, as the largest contributions to the effective exchange constants are found for radii smaller than $1.5a$ lattice spacings [17,33].

IV. RESULTS

A. Lattice relaxation

The total energy $E(c/a)$ as a function of the c/a ratio was calculated, and the results are shown in Figs. 2–5. The energy zero is defined with respect to the cubic parent compound, and consequently, the energy differences for all phases can be compared easily. The case of Mn_3Ga is used as a benchmark and is repeatedly plotted in Figs. 2 and 3. Table II contains the numerically optimized lattice parameters. The study reveals that a large number of the materials treated herein are most stable in their respective tetragonal structures, with $c/a > \sqrt{2}$.

Tetragonally compressed structures are described by $c/a < \sqrt{2}$, whereas tetragonally elongated lattices are characterized by $c/a > \sqrt{2}$, as compared to the cubic parent or austenite phase. Elongation occurs with an increase in the length of the c axis, whereas the ab plane is compressed, leaving the volume approximately unchanged. In this study, the volume of the unit cell V_{cell} was optimized in addition to the c/a ratio, and it was found that no significant change occurred for most cases (Table III).

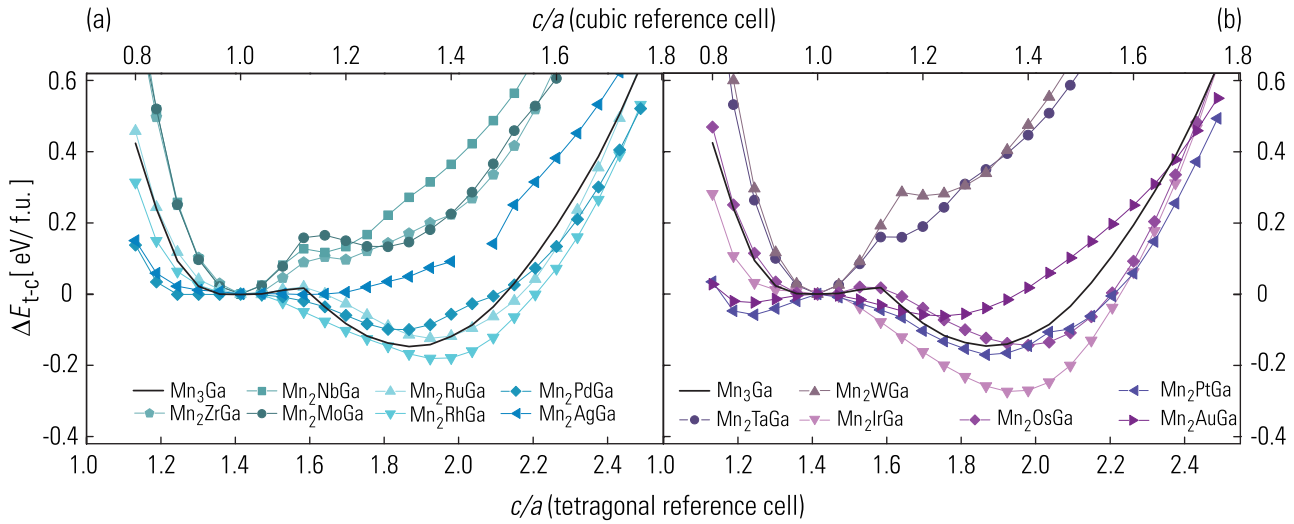

FIG. 3. (Color online) Energetic response to volume-conserving elongations and compressions of the crystal structure along the c axis for (a) the $Mn_2Y^{(4d)}Ga$ and (b) $Mn_2Y^{(5d)}Ga$ series. Systems involving late transition metals and systems exhibiting at least a local tetragonal energy minimum are shown.

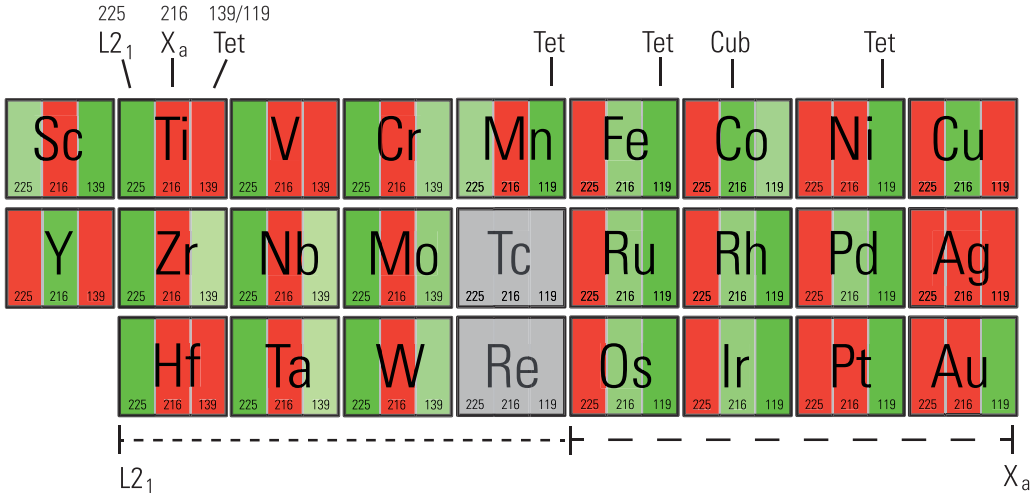

FIG. 4. (Color online) Schematic overview of the preferred site occupancy and crystal structure of Mn_2YGa Heusler compounds. Stable, metastable, and instable lattices are marked by dark-green, light-green, and red subcells, respectively.

Figures 2(a) and 2(b) show the $E(c/a)$ curves of the $Mn_2Y^{(3d)}Ga$ series for early transition metals (ETM; Y = Sc,Ti,V,Cr) and late transition metals (LTM; Y = Mn,Fe,Co,Ni,Cu), respectively. A preference for tetragonal structures is seen for materials including LTM for $Mn_2Y^{(3d)}Ga$, with Y being Mn, Fe, or Ni. In the group of ETM systems, Mn_2ScGa was found to be tetragonal, which is an exception. The situation for $Mn_2Y^{(4d)}Ga$ and $Mn_2Y^{(5d)}Ga$ is seen to be similar.

In contrast to Mn_2CoGa, for which a cubic structure ($c/a = \sqrt{2}$) is preferred, the systems with the same valence electron count ($N_V = 26$) involving heavier species (ruthenium and osmium) exhibit a global energy minimum for the tetragonal structure.

Discontinuities in the $E(c/a)$ curves are observed for the cases of Mn_3Ga and Mn_2FeGa, resembling a first-order transition, whereas $E(c/a)$ for Mn_2NiGa is continuous [Fig. 2(b)]. Strongly composition-dependent modulated martensitic phases [34,35] and premartensitic phases [36,37] have been experimentally produced; in combination with first-principles calculations [38], the onset of the martensitic transition has been thought to be initiated by a displacement of atomic planes orthogonal to the crystallographic c axis of the tetragonal cell. Experimentally [37] and theoretically [38], it has been shown that phonon softening along $[\zeta,\zeta,0]$ exists in shape-memory materials, and thus the transition has been related to the occurrence of the tetragonal distortion.

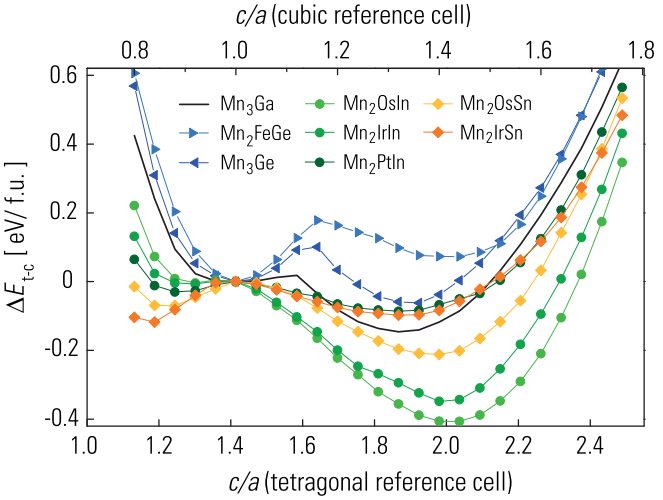

FIG. 5. (Color online) The energy landscapes $E(c/a)$ of Mn_3Ge, Mn_2FeGe, Mn_2(Ir,Pt)Sn, and Mn_2(Ir,Pt)In are shown.

In the current study, it was found that elongated tetragonal variants ($c/a > \sqrt{2}$) exist for all compounds that were unstable towards a tetragonal distortion and that these alloys were almost exclusively found, with the exception of Mn_2ScGa, in the compounds that exhibit *inverse*-type ordering (LTM compounds), as depicted in Fig. 4. In contrast, compressed variants possessing a global energy minimum were not observed in the Mn-Ga Heusler family.

The calculated lattice data and Figs. 2 and 3 lead to the conclusion that stable tetragonal structures may be formed only in the series of Mn_2YGa that includes LTMs, making them derivatives of inverse Heusler systems. The information obtained from the lattice optimization in terms of the relative positions of the energy minima is condensed in Fig. 4, which gives the preferred crystal structure visualized in the manner of the periodic table.

Each compound in the family of Mn_2YGa materials shown in Fig. 4 is depicted by one cell that symbolizes a transition metal Y of the $3d$,$4d$, or $5d$ series. The corresponding cell is built up by three subcells, which represent the two variants of chemical coordination (the first and second subcells) and the existence of a global energy minimum for $c/a \neq \sqrt{2}$ (third subcell). The color code symbolizes the energy levels of a configuration on the energy landscape relative to one another: dark green indicates a global minimum, light green represents a local minimum, and red means no minimum. In cases in which the investigated materials did not exhibit a cubic minimum, the first two subcells are understood to be the type of coordination around the $4d$ crystallographic site: the symmetry of the coordinating shell is either centrosymmetric

TABLE II. Calculated lattice parameters of the cubic parent phases and corresponding tetragonal structures compared with examples from existing literature data. The lattice parameters a and c are indexed to refer to the symmetry of the structure they represent. For the cubic case, which can be represented as equivalent descriptions, both representations are given, where $a_{\mathrm{cub}} = c_{\mathrm{tet}} = \sqrt{2}a_{\mathrm{tet}}$, as depicted in Fig. 1. The literature data are given in a similar format. The lattice parameters are given in angstroms. The total spin moment M_{spin} is given in units of μ_{B}/f.u. The listed literature data refers to resulting (R_m) cubic (C_m) or tetragonal (T_m) phases, that were investigated by theoretical ($m = t$) or experimental ($m = e$) methods m as indicated by the indices. The chemical order (chem. ord.) is approximated and specified in the order of the Wyckoff positions, "4*d* 4*c* 4*b* 4*a*", where parentheses indicate a mixed occupation.

		Cubic phases					Tetragonal phases					Literature data						
	N_V	SG	c/a	a_{cub}	a_{tet}	M_{spin}	SG	c/a	a_{tet}	c_{tet}	M_{spin}	SG	c/a	a_{tet}	c_{tet}	R_m	Chem. ord.	Reference
Mn_2ScGa	20	225	$\sqrt{2}$	6.15	4.35	–4.00	139	1.94	3.98	7.70	–5.36							
Mn_2TiGa	21	225	$\sqrt{2}$	5.95	4.21	–2.97	139					225	$\sqrt{2}$		5.95	C_t	MnMnTiGa	[43]
Mn_2VGa	22	225	$\sqrt{2}$	5.82	4.12	–1.98	139					225	$\sqrt{2}$		5.91	C_e	MnMnVGa	[44,45]
Mn_2CrGa	23	225	$\sqrt{2}$	5.76	4.07	–1.00	139	1.82	3.82	6.95	–2.75	225	$\sqrt{2}$		5.77	C_t	MnMnCrGa	[46]
Mn_3Ga	24	225	$\sqrt{2}$	5.82	4.12	0.01	139	1.82	3.90	7.08	–1.89	139	1.77	3.77	7.16	T_t	MnMnMnGa	[4]
												139	1.82	3.90	7.09	T_e	MnMnMnGa	[4]
Mn_2FeGa	25	216	$\sqrt{2}$	5.79	4.09	1.03	119	1.98	3.68	7.29	–0.78	119	1.90	3.79	7.19	T_e	$Mn(Fe,Mn)_2Ga$	[18]
Mn_2CoGa	26	216	$\sqrt{2}$	5.78	4.09	2.00	119	1.93	3.71	7.14	0.17	216	$\sqrt{2}$		5.86	C_e	MnCoMnGa	[47]
Mn_2NiGa	27	216	$\sqrt{2}$	5.85	4.14	1.18	119	1.82	3.79	6.91	1.00	216	$\sqrt{2}$		5.91	C_e		[48]
												119	1.72	3.91	6.70	T_e		[48]
												225	$\sqrt{2}$		5.94	C_e	$(Mn,Ni)_2MnGa$	[41]
												139	1.74	3.89	6.77	T_e	$(Mn,Ni)_2MnGa$	[41]
												216	$\sqrt{2}$		5.84	C_t	MnNiMnGa	[39]
Mn_2CuGa	28	216	$\sqrt{2}$	5.94	4.20	0.33						216	$\sqrt{2}$		5.94	C_t	MnCuMnGa	[39]
Mn_2ZrGa	21	225	$\sqrt{2}$	6.14	4.34	–3.00	119											
Mn_2NbGa	22	225	$\sqrt{2}$	6.00	4.24	–2.00	119											
Mn_2MoGa	23	225	$\sqrt{2}$	5.91	4.18	–1.01	119	1.81	3.89	7.04	–2.99							
Mn_2RuGa	25	216	$\sqrt{2}$	5.96	4.22	1.03	119	1.96	3.80	7.45	–0.24	216	$\sqrt{2}$		6.00	C_e	$(Mn_{\frac{2}{3}},Ru_{\frac{1}{3}})(Ru_{\frac{2}{3}},Mn_{\frac{1}{3}})MnGa$	[19]
Mn_2RhGa	26	216	$\sqrt{2}$	5.98	4.23	1.64	119	1.94	3.82	7.43	0.10	225	$\sqrt{2}$		6.03	C_e	$(Mn,Rh)_2MnGa$	[20]
Mn_2PdGa	27	216	$\sqrt{2}$	6.12	4.33	0.55	119	1.84	3.93	7.23	0.93							
Mn_2AgGa	28	216	$\sqrt{2}$	6.22	4.40	0.34	119											
Mn_2HfGa	21	225	$\sqrt{2}$	6.12	4.33	–2.99	119											
Mn_2TaGa	22	225	$\sqrt{2}$	6.00	4.24	–1.99	119											
Mn_2WGa	23	225	$\sqrt{2}$	5.92	4.19	–0.94	119											
Mn_2OsGa	25	216	$\sqrt{2}$	5.95	4.21	1.02	119	1.97	3.80	7.48	–0.28							
Mn_2IrGa	26	216	$\sqrt{2}$	5.97	4.22	2.00	119	1.95	3.83	7.44	0.11							
Mn_2PtGa	27	216	$\sqrt{2}$	6.13	4.33	0.44	119	1.87	3.91	7.31	0.75	119	1.38	4.37	6.05	T_e	MnPtMnGa	[21]
Mn_2AuGa	28	216	$\sqrt{2}$	6.26	4.42	0.19	119	1.73	4.11	7.13	0.14							
Mn_2OsSn	25	216	$\sqrt{2}$	6.21	4.39	1.50	119	1.95	3.97	7.75	–0.02							
Mn_2IrSn	26	216	$\sqrt{2}$	6.31	4.46	0.41	119	1.91	4.01	7.67	0.45	119	1.54	4.29	6.59	T_e	MnIrMnSn	[49]
Mn_2PtSn	27	216	$\sqrt{2}$	6.39	4.52	0.19	119	1.81	4.15	7.52	–0.02	119	1.35	4.51	6.08	T_e	MnPtMnSn	[1]
Mn_2OsIn	25	216	$\sqrt{2}$	6.26	4.43	0.62	119	2.02	3.93	7.93	–0.27							
Mn_2IrIn	26	216	$\sqrt{2}$	6.30	4.45	0.68	119	1.98	3.97	7.85	0.07							
Mn_2PtIn	27	216	$\sqrt{2}$	6.37	4.51	0.31	119	1.84	4.12	7.57	0.38	119	1.57	4.32	6.77	T_e	MnPtMnIn	[23]
Mn_3Ge	25	216	$\sqrt{2}$	5.76	4.07	1.01	119	1.90	3.74	7.10	–0.98	225	1.91	3.81	7.26	T_e	MnMnMnGe	[50]
												225	1.90	3.75	7.12	T_t	MnMnMnGe	[6]
Mn_2FeGe	26	216	$\sqrt{2}$	5.73	4.05	2.01	119	2.05	3.63	7.42	–0.06	216	$\sqrt{2}$		5.80	C_t	MnFeMnFe	[51]

(in relation to SG 225) or noncentrosymmetric (in relation to SG 216). As shown in a preceding publication on the cubic variants [17], systems involving ETMs adopt the $L2_1$-type structure, whereas compounds containing LTMs are found to have the inverse Heusler structure (X_a type).

Inspection of Fig. 4 in combination with Figs. 2 and 3 reveals interesting details, such as the fact that tetragonal derivative phases of cubic Heusler alloys, which imply that a global energy minimum is present, are observed only for a valence electron count of $N_V \geqslant 24$. It is also clearly seen that the onset of the formation of tetragonally elongated structures evolves over the periods from left to right and from lower to higher N_V. This leads to the question of the mechanism behind this distortion, which we are going to approach in Sec. IV A 1.

The lattice parameters for all cubic compounds are found within a range of $\Delta a_{c/\sqrt{2}} = 0.35$ Å for the Ga series. The values increase from the borders of the series towards the middle of the range. The same behavior is found for tetragonal compounds, where the range spans from $a_{\mathrm{tet}} = 3.68$ to 4.11

TABLE III. Relative volume change between the cubic and tetragonal phases, $C_{t/c} = (V_{tet} - V_{cub}) \times 100/V_{cub}$.

Material	$C_{t/c}$ (%)	Material	$C_{t/c}$ (%)
Mn_2ScGa	5.08	Mn_2OsGa	2.32
Mn_2CrGa	6.11	Mn_2IrGa	2.44
Mn_3Ga	9.08	Mn_2PtGa	–3.13
Mn_2FeGa	1.93	Mn_2AuGa	–1.49
Mn_2CoGa	1.82	Mn_2OsSn	
Mn_2NiGa	–1.09	Mn_2IrSn	–1.94
Mn_2CuGa	2.37	Mn_2PtSn	–0.35
Mn_2MoGa	3.46	Mn_2OsIn	–0.36
Mn_2RuGa	1.63	Mn_2IrIn	–1.01
Mn_2RhGa	1.48	Mn_2PtIn	–0.86
Mn_2PdGa	–2.78	Mn_3Ge	3.98
		Mn_2FeGe	3.80

($\Delta a_{tet} = 0.43$ Å) and $c_{tet} = 6.91$ to 7.48 ($\Delta c_{tet} = 0.54$ Å), whereas Mn_2ScGa is an exception. The c/a coordinate exhibits inverted behavior, decreasing from the middle to the left and right borders of the series. The overall similarity of the lattice data opens the possibility of intermiscibility with each other and thus tunability of the whole class of materials. Therefore the magnetization may be adjusted over a large range, allowing for the formation of tetragonal compensated ferrimagnets via adequate substitution.

Having discussed the structural trends as a function of the valence electron change in the d-electron system, the effects of the variation of the main group element, Z, from Ga to Ge, In, and Sn in a small sample of compounds [Mn_2(Mn,Fe)Ge, Mn_2(Os,Ir,Pt)In, and Mn_2(Os,Ir,Pt)Sn] are briefly discussed. The corresponding data, including those for Mn_3Ga, are graphed in Fig. 5.

Figure 5 reveals that the placement of In and Sn at the Z position leads to the emergence of a deep energy minimum for Mn_2IrSn with $c/a < \sqrt{2}$ and even deeper minima for elongated phases with large c/a ratios for Mn_2OsIn, Mn_2IrIn, and Mn_2OsSn, whose lattice parameters resemble those of layered structures. Heusler alloys are often interpreted in terms of a rigid, band-model-like approach, and an electron-filling scheme is employed for the prediction of magnetic moments in Co_2-based alloys. Interpretation of the tetragonal instabilities using such an approach leads to the assumptions of Mn_3Ge ($N_V = 25$) behaving analogously to Mn_2FeGa ($N_V = 25$) and of Mn_2FeGe ($N_V = 26$) being similar to Mn_2CoGa ($N_V = 26$). A comparison of the corresponding c/a curves demonstrates that this is approximately true and thus that isoelectronicity is an appropriate concept in the chemistry and physics of Heusler materials.

Although our calculations agree well with those of previous works [9,39,40], a comparison with the experimental data of Mn-Ni-Ga systems exhibits an interesting discrepancy. The deviation between experiment and theory was traced back to the deviating structural model in terms of the occupation of the involved sites. Neutron diffraction studies on Mn_2NiGa highlighted the fact that the order is different from the expected X_a type in the austenite phase. Thus the chemical formula reads (Mn,Ni)$_2$MnGa and is called the $L2_{1b}$ type because the point symmetry includes inversion symmetry through random occupation of 4d and 4c sites with Ni and Mn [41]. Similarly, in Mn_2FeGa, a deviation from theory was found in an experimental study because the site occupation was expected to differ from the perfect MnFeMnGa ordering [18]. Similar issues are present for the $Mn_2Y^{(4d)}Ga$ series. From available data, including neutron diffraction studies, the site occupancies have been clarified. Several authors found members of the Mn_2RuZ series (Z = Ga,Ge,Si,Sn) and Mn_2RhZ series (Z = Ga) [19,20,42] not to be tetragonal under the respective reaction conditions. In contrast, they have been realized as cubic Heusler alloys exhibiting a strong degree of antisite disorder, which has been characterized as an alloying tendency [20].

Orthorhombic deformations of the unit cell have been observed in some systems such as Mn_2NiGa [39]. Thus the restriction to tetragonal distortions and ordered compounds in conducted studies leads to a simplified description of these materials. Nevertheless, a general understanding can be obtained in approaching the Mn_2-based Heusler systems through this ansatz. In future studies that aim to predict ground-state structures and magnetic configurations, the parameter space for the atomic sites and relaxation paths for the electronic and spin degrees of freedom have to be enlarged, and restrictions that are widely used have to be dropped. As a consequence of the applied restrictions, disorder effects were not incorporated into this study, thus leaving open any explanations of the deviations from experimental results.

1. *Analysis of the densities of states*

Various attempts to explain the instability of the cubic phase have been given in the literature using models such as the band Jahn-Teller effect [5,18], anomalous phonon vibrations [40,52,53], and Fermi-surface nesting [54]. These different approaches describe the same behavior, i.e., the instability of the cubic phase, from different perspectives and extract different types of information. Commonly, the densities of states (DOSs) of related cubic and tetragonal phases are compared and contrasted marking the starting and end points of the transition. As an example for the $Mn_2Y^{(3d)}Z$ series, the DOSs of Mn_3Ga, Mn_2FeGa, and Mn_2NiGa are shown in Figs. 6–8. For the cubic variants, the partial DOSs (PDOSs) are shown in their corresponding projections on the sites and in terms of projections on the irreducible representations. The peaks in the PDOS of Mn(4b) are well separated on the energy scale. On the one hand, this separation is due to the strong crystal-field splitting of the Mn(4b) d states, where the occupied e_g states are located in a range between -4 and -3 eV, whereas the t_{2g} PDOS is found between -1 eV and the Fermi edge ε_F. On the other hand, the separation of occupied and empty states follows from the strong exchange split of the Mn(4b) d states, in contrast to the d states of Y(4c) and Mn(4d), which are found to be more widely dispersed even though the majority and minority states are separated owing to exchange splitting. The PDOSs of Mn(4d) and Y(4c) are strongly dispersed, with considerable overlap of the spectral weight between the t_{2g} and e_g states in the majority channel, whereas the minority channel is gapped, with t_{2g} characterizing the lower boundary and e_g comprising

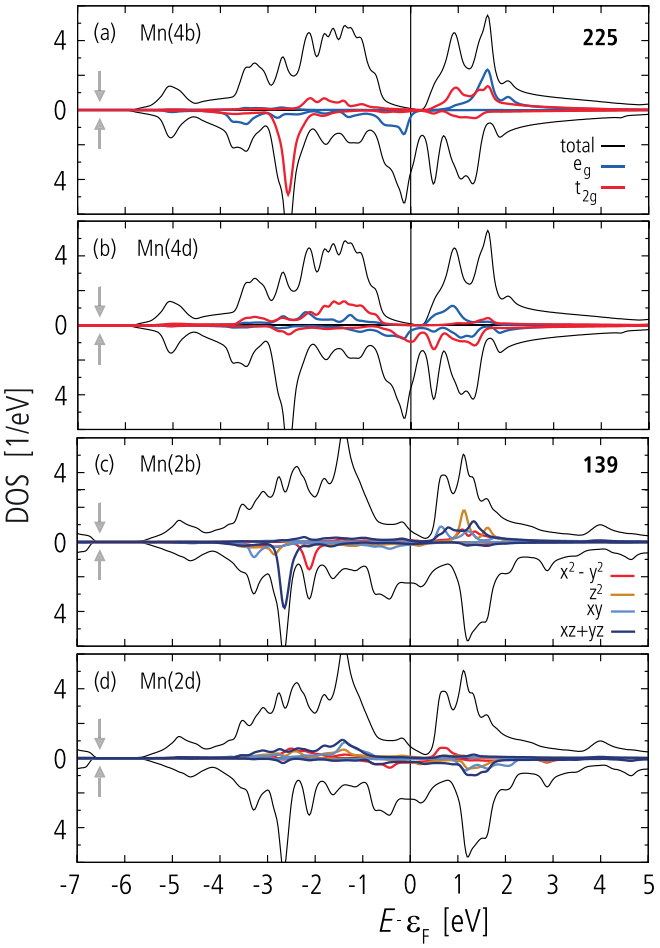

FIG. 6. (Color online) DOS of cubic (SG 225) and tetragonal (SG 139) Mn_3Ga.

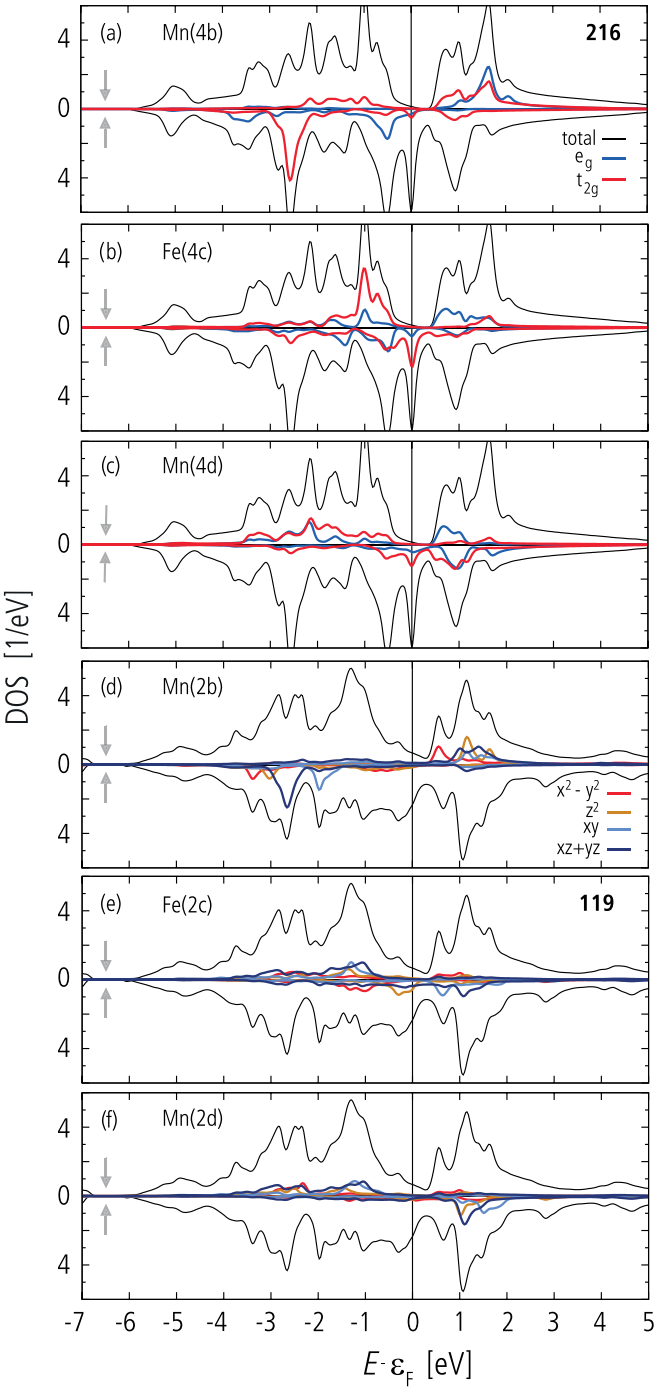

FIG. 7. (Color online) DOS of cubic (SG 216) and tetragonal (SG 119) Mn_2FeGa.

the upper boundary of the gap. As the DOS is gapped in the minority-spin channel, the study of the tetragonal system is strongly facilitated as the states at the Fermi edge in the majority channel mostly constitute the origin of the tetragonal distortion. The majority PDOSs in the range of -5 eV up to ε_F exhibit a characteristically shaped peak structure. From Mn_3Ga to Mn_2CoGa, the majority-spin channel [bottom panels of Figs. 6(a)–8(c)] is continuously filled. The Fermi energy is consequently shifted to higher band energies, and thus ε_F sweeps over a range of the majority DOSs, whereas the minority-spin channel remains unchanged. It is clearly seen from Figs. 6 and 7 that the tetragonal transition correlates with the peak structure of the majority DOSs. If ε_F is centered on a peak of the majority DOS, the tetragonal distortion can be triggered. These local maxima are mainly composed of states of the $Y(4c)$ (Mn, Fe, Co, Ni) and Mn($4d$) atoms. These energy levels are mainly of t_{2g} symmetry. In simple interpretation, the DOS can be understood in a rigid-band-like fashion. The limit of this interpretation is reached with Mn_2NiGa, where the d PDOS is rearranged and the Slater-Pauling rule is no longer valid for the cubic phase [17]. Comparing this to the PDOS of the tetragonally distorted systems, it is observed that the resulting PDOSs are widely dispersed and significantly less structured. Mn_2NiGa, however, behaves differently. Further filling of the majority states, as intuitively expected, does not occur. In contrast, the gap in the minority channel closes as the states with e_g symmetry are pulled towards ε_F. Thus the tetragonal distortion in Mn_2NiGa is formed by another mechanism, which may explain why Mn_2NiGa is found to be a magnetic shape-memory alloy, whereas Mn_3Ga and Mn_2FeGa are found in their respective tetragonal crystal structures, although the total energy differences are comparable to that of Mn_2NiGa.

We emphasize that these findings differ from other models in which the instability is thought to depend solely on states of

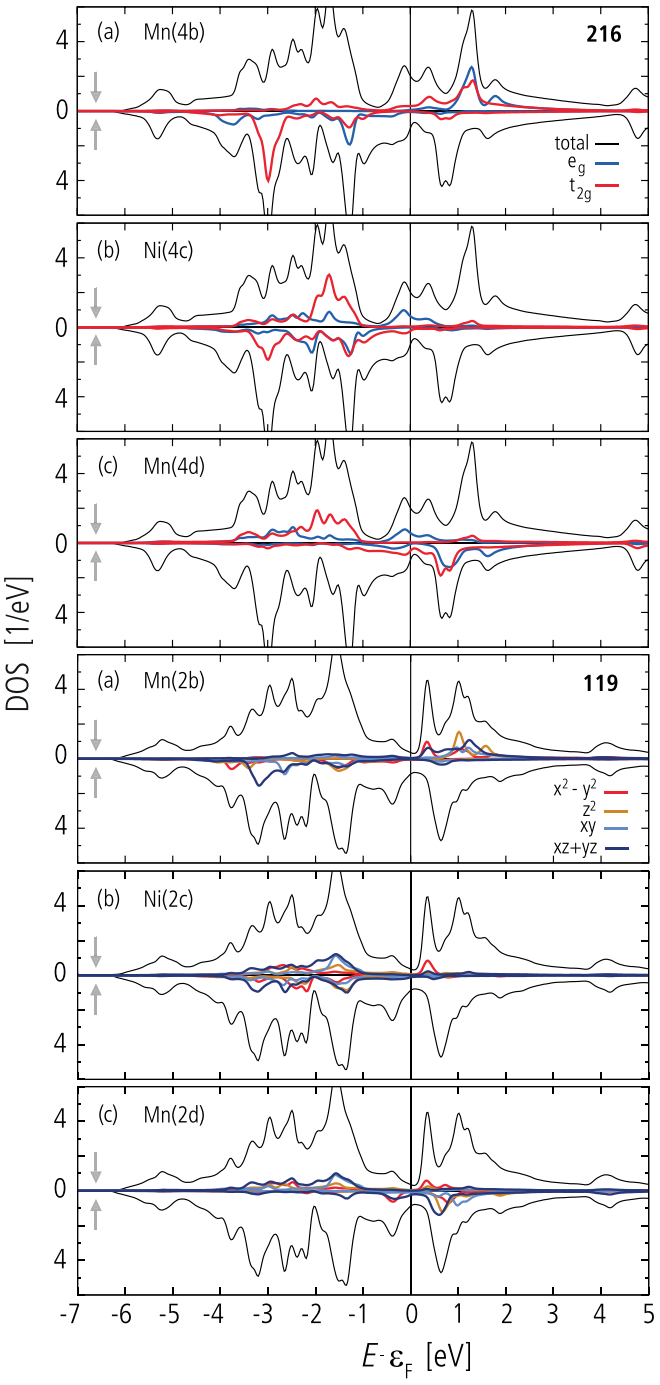

FIG. 8. (Color online) DOS of cubic (SG 216) and tetragonal (SG 119) Mn_2NiGa.

Mn(4*b*) that is found in a tetrahedral environment. The DOS at ε_F is mainly composed of states of the 4*c* and 4*d* positions with minor contributions from Mn(4*b*). Here the instability removes the strong peaks of Mn, Fe, and Co at the 4*c* position, whereas the states of Mn(4*b*) are not rearranged.

2. Spin polarization

Half-metallicity [55,56] [complete or nearly complete spin polarization $P(\varepsilon_F) \approx 100\%$] is generally observed in cubic Co_2- and Mn_2-based Heusler compounds. The highly

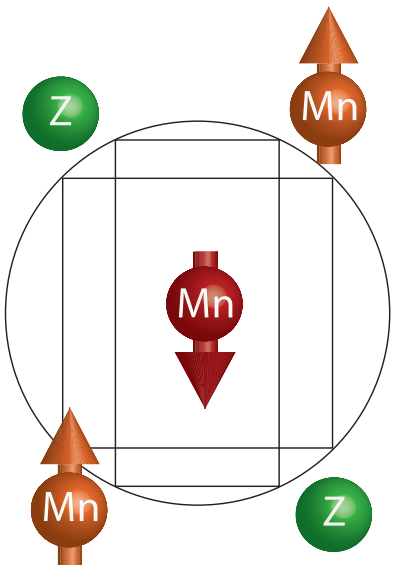

FIG. 9. (Color online) A two-dimensional projection of the nearest-neighbor coordination of Mn(4*b*) is shown. The symmetry of the coordination changes while undergoing the *martensitic transition*, whereas the nearest-neighbor distance remains unchanged as the volume change is on the order of only 1%–9%.

symmetric structure and the peculiar electronic properties due to covalent bonding lead to the appearance of a gap in the minority DOS. The emergence of the tetragonal distortion reduces the spin polarization of the half-metallic cubic parent phases. The degeneracy of the t_{2g} and e_g states is lifted due to the change in local coordination caused by the distortion, which is seen in Figs. 6–9, and the emergence of a *pseudogap* in one spin channel is observed instead.

B. Magnetic ground state

1. The Slater-Pauling rule

Referring to a previous publication [17] on the cubic parent compounds of the investigated materials, the results are presented by means of the Slater-Pauling curves. As can be seen in Fig. 10, the Slater-Pauling rule experiences strong changes, so calling it the Slater-Pauling rule is done for reasons of convenience. Figure 10 visualizes the fact that the magnetization of all tetragonal alloys of the $Mn_2Y^{(d)}Ga$ family experience a shift to smaller values. In the case of the $Mn_2Y^{(3d)}Ga$ group, this shift is found to be constant throughout the set of compounds, which results in a linear dependence of the net moment on the valence electron count, thus giving rise to *pseudo-Slater-Pauling* behavior, even though half-metallicity and thus integer net moments are not observed (Fig. 11). A decrease in the net moment is also found for the $Mn_2Y^{(4d)}Ga$ and $Mn_2Y^{(5d)}Ga$ compounds. Unlike the lighter compounds, the changes are not constant over the series and therefore result in nearly vanishing net moments for Mn_2RuGa, Mn_2RhGa, Mn_2PdGa, Mn_2OsGa, Mn_2IrGa, Mn_2PtGa, and Mn_2AuGa, as is seen in Fig. 10. Nevertheless, compensation of spin moments may be achieved for an electron count close to $N_V = 25.7$, which can be realized by intermixtures of stoichiometric phases of Mn_2YGa,

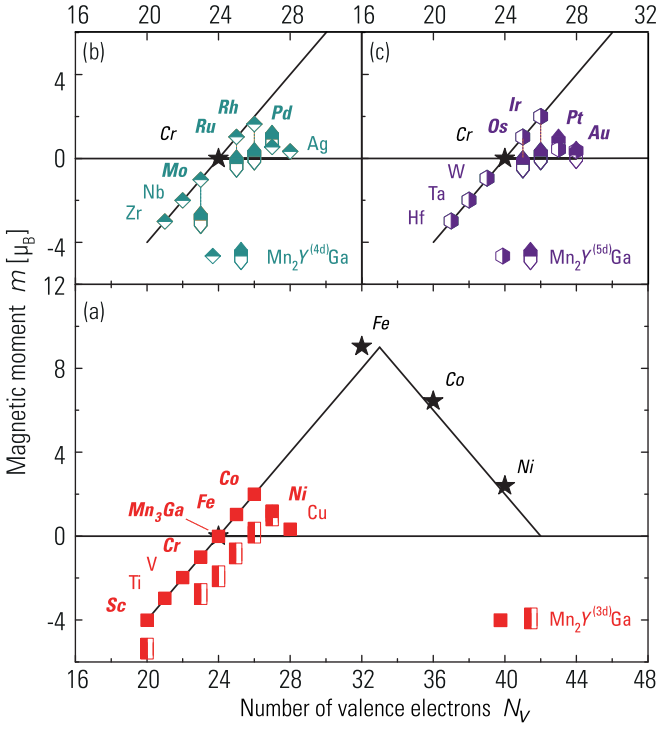

FIG. 10. (Color online) Slater-Pauling curves of (a) $Mn_2Y^{(3d)}Ga$, (b) $Mn_2Y^{(4d)}Ga$, and (c) $Mn_2Y^{(5d)}Ga$ compounds.

such as $m_{Mn_3Ga} = -1.89\mu_B$ and a corresponding proportion of Mn_2NiGa with $m_{Mn_2NiGa} = 1.00\mu_B$ or Mn_2CoGa. Thus fractions of $0.435m_{Mn_2NiGa}$ and $0.565m_{Mn_2FeGa}$ could ideally lead to complete compensation of the magnetization. A similar approach was undertaken by Nayak *et al.*, who obtained a compensated ferrimagnet by varying the Mn/Pt ratio in $Mn_{3-x}Pt_xGa$, leading to complete compensation of magnetization for $x \approx 0.59$ theoretically [22]. In Mn_2Ru_xGa thin films the compensation of the spin moment has been achieved through variation of the ruthenium concentration [57].

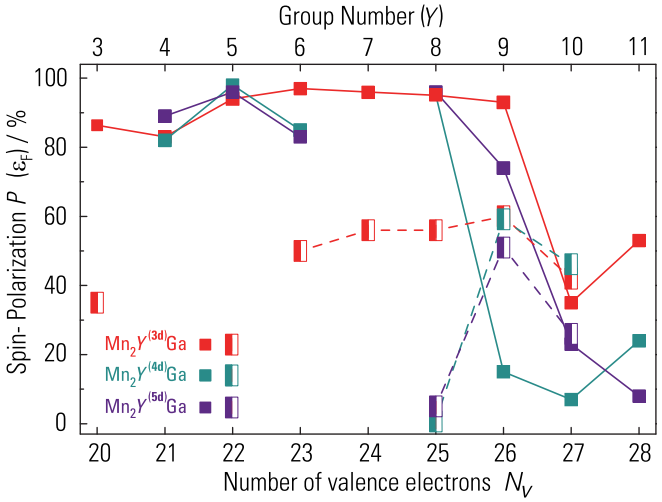

FIG. 11. (Color online) The spin polarization at the Fermi energy for both cubic and tetragonal phases. For a system with $N_V < 27$, the spin polarization is reduced by the tetragonal distortion.

2. *Local magnetic moments*

The change in the total magnetic moment should be understood in terms of the site moments. Inspection of Fig. 12 clearly reveals the dependencies. The change in the local moments indicates the specific impact of the distortion on the single sites. The local moments responding most strongly to elongation/compression of the crystal axes are members of the magnetic sublattices formed by the Mn($8c$), Mn($4d$), and Y($4c$) sites (the former so-called *tetrahedral* sites compared to SG 225). Depending on the characters of the local moments, which are either itinerant or localized in nature [14,55], we find major differences in the influence of the tetragonal distortion on these sites. In Fig. 12, the localized moment of Mn($4b$) is found in the upper part of the plot for a positive value of the magnetic moment of approximately $3\mu_B$. The effect of elongation along the c axis and compression of the ab plane has a stronger influence on moments of itinerant character found in the lower part of the plot, referring to the $4d$ and $4c$ sites. These are located in the same lattice plane (compare the atoms depicted as red and blue spheres in Fig. 1). Manganese on site $4b$ [Mn($4b$)] exhibits a large localized moment of $3\mu_B$ and thus is generally much less affected. Apart from the magnitude of the local moments, Fe($4c$) in Mn_2FeGa exhibits a spin flip from parallel to antiparallel alignment of the Mn($4b$)-Fe($4c$) interaction upon the tetragonal distortion. Apart from the changes in magnitude of the local atomic moments, the effective antiparallel coupling of the nearest-neighbor manganese atoms does not suffer from the structural transformation, as quantified in terms of the exchange interaction constants in Sec. IV C. Since the volume change $C_{t/c}$ is on the order of 1%–2% for most systems, the nearest-neighbor distance basically does not change, whereas the direction of the nearest-neighbor interaction does (Fig. 9). In the case of Mn_3Ga, $C_{t/c}$ is approximately 9% and thus may suppress the shape-memory effect in this material.

3. *Magnetocrystalline anisotropy*

Inherent in noncubic crystals is a directional preference of magnetization that is absent in cubic materials, which is related to the tetragonal modification of the crystal axes. The MCA energy is computed as described in Sec. III.

The anisotropy energy is phenomenologically thought to depend on the value of the c/a ratio, which is more or less equal for most of the compounds investigated in the present study. Therefore the underlying mechanism is understood as a band-filling effect, which affects the spin-orbit coupling (SOC) symmetry. This interpretation can directly be taken from Figs. 13(a) and 13(b) (see Table IV). Increasing the SOC strength by varying the Y element through the $3d$, $4d$, and $5d$ series increases the MCA energy by a factor of approximately 3 for Y = Fe, Ru, Os. The effect of band filling is deciphered by sweeping the Y elements along a series. Going from left to right in any set of compounds $Mn_2Y^{(3d,4d,5d)}Ga$, the MCA is altered from preferred *out-of-plane* to *in-plane* orientation. The same situation holds for $Mn_2Y^{(5d)}Z$ compounds, whose preferred orientation is graphed in Fig. 13(b). Three compounds in Fig. 13 deserve special attention: Mn_2RhSn, Mn_2PtIn, and Mn_2IrSn. Previously, Mn_2PtIn and Mn_2IrSn were predicted to possess a noncollinear magnetic order just like Mn_2RhSn,

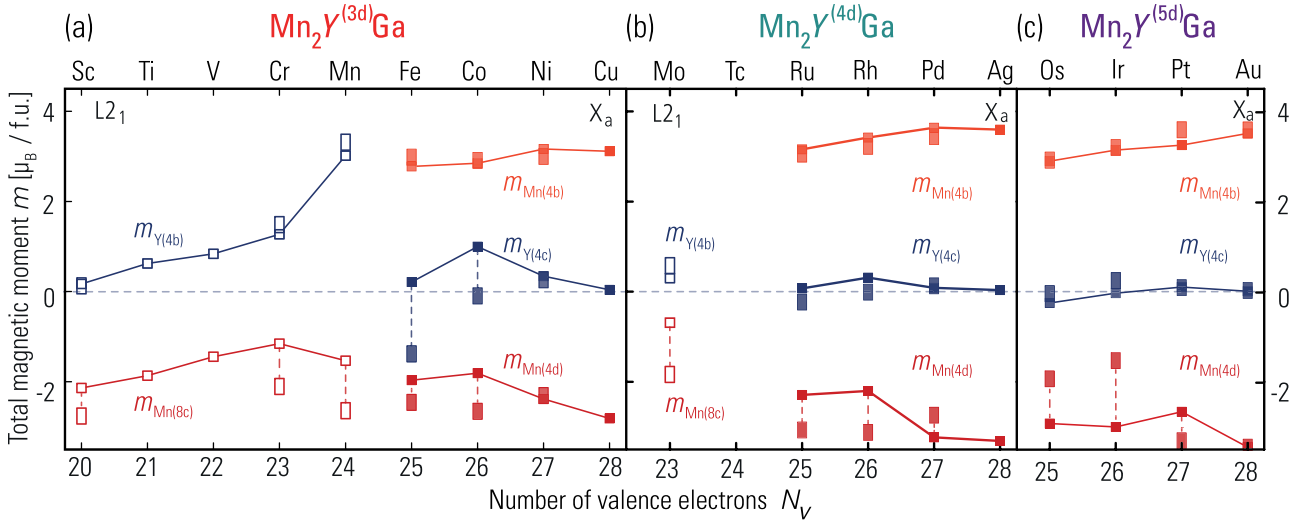

FIG. 12. (Color online) Atomic magnetic moments in (a) $Mn_2Y^{(3d)}Ga$, (b) $Mn_2Y^{(4d)}Ga$, and (c) $Mn_2Y^{(5d)}Ga$ compounds. Open symbols denote the $L2_1$-type coordination. Solid symbols denote the X_a-type coordination. The squares stand for the cubic materials, whereas the tetragonal systems are represented by rectangles.

which was investigated experimentally and theoretically in great detail in Ref. [49]. The MCA for Mn_2RhSn is seen in Fig. 13(b) and Table IV to be barely in plane, whereas, experimentally, it is out of plane. It is the Mn atom at site 4*d* which by means of canting supplies the energy in favor of the spin reorientation. Although we did not consider noncollinear order in the present study, we can state that Mn_2RhSn and most likely Mn_2PtIn as well as Mn_2IrSn are cases in which a spin reorientation is accompanied by noncollinear order. The border cases in Fig. 13(a) may hide a comparable spin reorientation. Similar physics is observed in the famous rare-earth magnets $Nd_2Fe_{14}B$ and $Er_2Fe_{14}B$. Manganese thus shares properties with rare-earth elements [58–60].

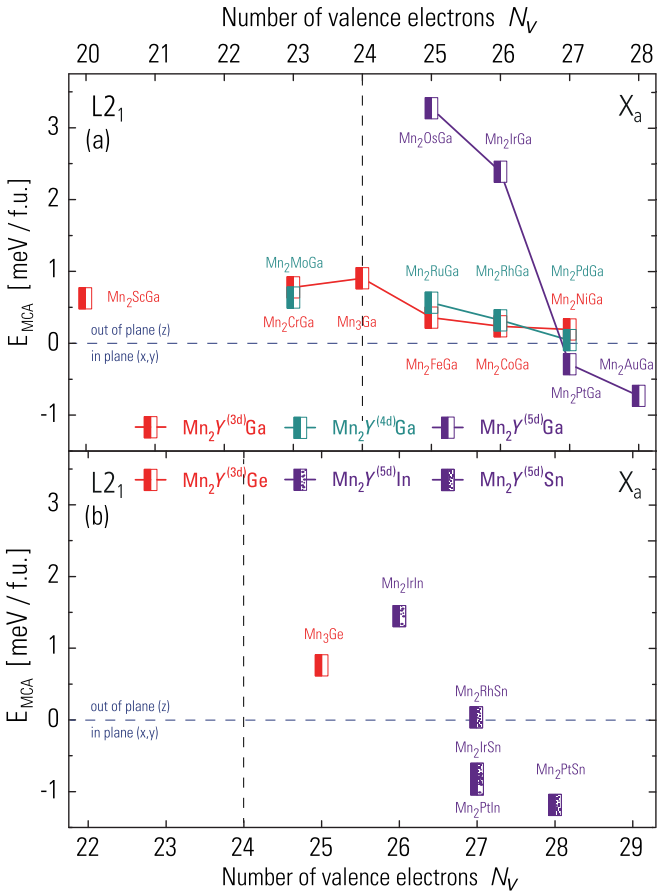

FIG. 13. (Color online) Calculated MCA energy of Mn_2YGa and some chosen Mn_2YZ alloys: Mn_3Ge, Mn_2RhSn, Mn_2IrIn, Mn_2IrSn, Mn_2PtIn, and Mn_2PtSn.

C. Exchange coupling and curie temperatures

The details of the calculations pertaining to Curie temperatures T_C have been described by us previously [17]. Even though the in-plane next-nearest-neighbor distance decreases due to the tetragonal distortion, the next-nearest-neighbor Mn(8*c*)-Mn(8*c*) coupling is still positive for the $L2_1$-derived tetragonal phases; thus the overall magnetic order does not change. A decrease or change of sign of the coupling constant $J_{\mathrm{Mn}(4d)\text{-}\mathrm{Mn}(4d)}$ is typical owing to preferential antiparallel

TABLE IV. Computed MCA energies. E_{MCA} represents the magnetocrystalline anisotropy energies (in meV/f.u.), and K_u is the anisotropy constant (in $\mathrm{MJ/m^3}$).

Compound	E_{MCA}	K_u	Compound	E_{MCA}	K_u
Mn_2CrGa	0.779	2.46	Mn_2OsGa	3.270	9.72
Mn_3Ga	0.906	2.70	Mn_2IrGa	2.388	7.02
Mn_2FeGa	0.359	1.16	Mn_2PtGa	–0.293	–0.84
Mn_2CoGa	0.236	0.77	Mn_2AuGa	–0.731	–1.94
Mn_2NiGa	0.193	0.62	Mn_3Ge	0.762	2.46
			Mn_2IrIn	1.447	3.75
Mn_2MoGa	0.636	1.91	Mn_2PtIn	–0.898	–2.24
Mn_2RuGa	0.564	1.68	Mn_2RhSn	0.053	0.17
Mn_2RhGa	0.322	0.95	Mn_2IrSn	–0.741	–1.93
Mn_2PdGa	0.040	0.11	Mn_2PtSn	–1.185	–2.93

TABLE V. The calculated Curie temperatures (in K) of tetragonal ($T_{C,t}$) and cubic ($T_{C,c}$) parent compounds (taken from Ref. [17]). The changes due to the tetragonal distortion are listed as $\Delta T_{C,t-c}$.

Compound	P_c	P_t	$T_{C,c}$	$T_{C,t}$	$\Delta T_{C,t-c}$	Compound	P_c	P_t	$T_{C,c}$	$T_{C,t}$	$\Delta T_{C,t-c}$	Compound	P_c	P_t	$T_{C,c}$	$T_{C,t}$	$\Delta T_{C,t-c}$
Mn_2ScGa	87	35	464														
Mn_2TiGa	83	557				Mn_2ZrGa	82	207				Mn_2HfGa	89				
Mn_2VGa	94	587				Mn_2NbGa	98	289				Mn_2TaGa	96				
Mn_2CrGa	97	50	578	970	392	Mn_2MoGa	85	65	140	335	196	Mn_2WGa	83				
Mn_3Ga	96	56	221	610	389												
Mn_2FeGa	95	56	601	848	247	Mn_2RuGa	95	1	619	1315	696	Mn_2OsGa	96	5	273	1075	802
Mn_2CoGa	93	60	928	1124	196	Mn_2RhGa	15	59	576	1351	776	Mn_2IrGa	74	51	411	1122	711
Mn_2NiGa	35	42	1005	750	−255	Mn_2PdGa	7	46	809	335	−473	Mn_2PtGa	23	26	799	326	−472
Mn_2CuGa	53	1491				Mn_2AgGa	24	1240				Mn_2AuGa	8	16	1027	897	−130

coupling as resulting from short Mn-Mn distances. Instead, the cubic to tetragonal transition even results in increased values, thus leading to an increase in T_C (Fig. 14 and Table V). *Prima facie*, the overall trend of increased T_C cannot be traced back to a common mechanism. In contrast, there is no exchange interaction that exhibits a similar behavior over the series. For instance, the findings in the case of Mn_2FeGa are related to the reduction of magnetic frustration, which is due to the competing antiparallel Mn(4*b*)-Mn(4*d*) interaction and parallel interactions of Fe(4*c*) with both Mn(4*d*) and Mn(4*b*) neighbors. Upon the tetragonal distortion a spin flip of the Fe(4*c*) local moment is observed due to the change in the sign of the Mn(4*b*)-Fe(4*c*) interaction. Upon the distortion, the strength of the Mn(4*b*)-Mn(4*d*) interaction is altered by approximately $\Delta J_{Mn(4b)-Mn(4b)} = 56$ meV in Mn_2FeGa.

A similar, but smaller, effect is found in Mn_2CoGa, indicating the magnetic frustration that had been present in the cubic phase and the weakening of the exchange interaction $Y(4c)$-Mn(4*b*) (Y = Fe, Co) due to the tetragonal distortion. This might be one of the contributions prohibiting the shape-memory effect in Mn_2FeGa. The main contribution to T_C, the Mn(4*d*)-Mn(4*b*) exchange, does not suffer from the structural transition. Similarly, the influence of the distortion on the exchange causes the smaller contributions to be altered and some frustration to be diminished. For example, the Mn(4*d*)-Mn(4*d*) interaction vanishes, with preferred antiparallel alignment in the cubic case, whereas the major Mn(4*d*)-Mn(4*b*) interaction remains unchanged.

Exceptions to the general observation of increased T_C in tetragonally distorted phases are Mn_2NiGa, Mn_2PdGa, and Mn_2PtGa systems, in which the T_C are reduced upon the tetragonal distortion. The significant reduction (Fig. 14) is caused by a weakened Mn(4*d*)-Mn(4*b*) interaction (Fig. 15), which may indicate an unstable magnetic ground state. A relation to the Heusler compound Mn_2RhSn [49] can theoretically be established as these materials possess the same number of valence electrons N_V.

V. SUMMARY

Using total energy calculations within density functional theory, we investigated in detail the response to tetragonal distortions for a large set of cubic Heusler compounds, $Mn_2Y^{(3d,4d,5d)}Ga$, and some other chosen materials. We were

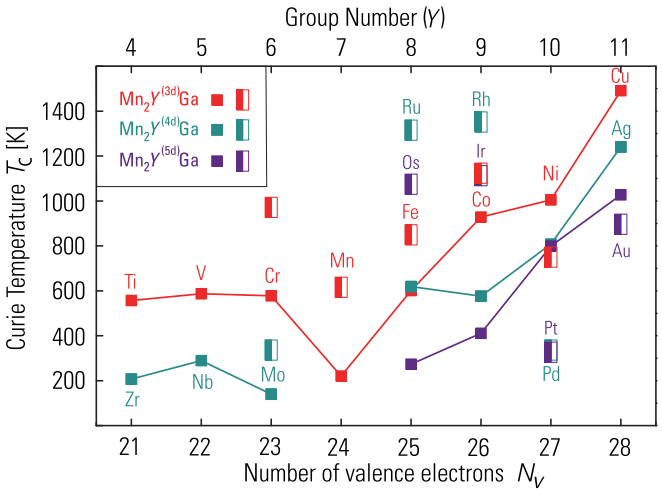

FIG. 14. (Color online) The calculated Curie temperatures of the Heusler compounds containing Ga. The results shown here are obtained using the mean-field approximation and highlight the consequence of the structural relaxation. Squares correspond to cubic compounds, and rectangles correspond to tetragonal compounds.

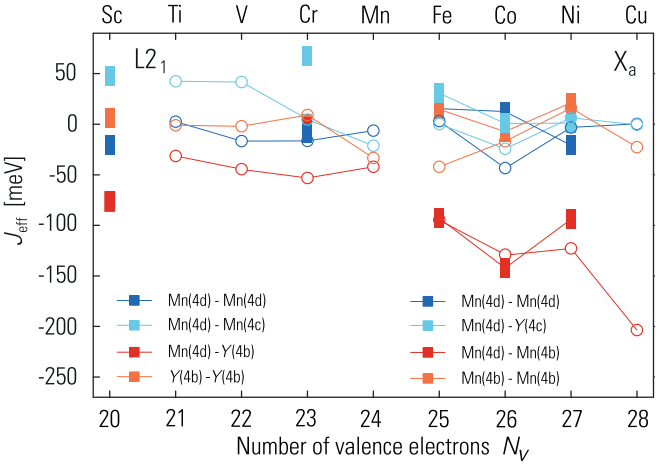

FIG. 15. (Color online) The evaluated effective exchange interaction parameters are shown and compared for the cubic and tetragonal structures of the $Mn_2Y^{(3d)}Ga$ series. Thus, the underlying mechanism of the increase of T_C due to the distortion is visualized. Circles correspond to cubic compounds, and rectangles correspond to tetragonal compounds.

able to single out the systems that remain cubic from those that favor a tetragonal structure. The details of the total energy as a function of the distortion were found to be similar for materials exhibiting the same number of valence electrons. The magnetizations of the tetragonal alloys were found to be shifted to smaller values, which we could attribute to changes of the itinerant local moments. This led to characteristic modifications of the Slater-Pauling curve. By means of partial densities of states, the changes to the electronic structures revealed the microscopic origin of the observed trends. Compared to the cubic parent phases, tetragonal structures exhibited a strengthening of the exchange interaction between neighboring sites and a weakening of competing interactions, which resulted in an increase of the Curie temperature. Focusing our attention on the magnetocrystalline anisotropy, we observed an interesting trend that describes a spin reorientation over our series of compounds; furthermore very large anisotropies are found for tetragonal Heusler compounds containing heavy transition metals accompanied by low magnetic moments, which indicates that these materials may be promising candidates for spin-transfer-torque applications.

ACKNOWLEDGMENTS

The authors gratefully acknowledge financial support from the Deutsche Forschungsgemeinschaft (DfG; Project P 1.2-A of research unit FOR 1464 “ASPIMATT”) and the European Research Council Advanced Grant (ERC-AG) No. 291472, “IDEA Heusler!”

[1] J. Winterlik, S. Chadov, A. Gupta, V. Alijani, T. Gasi, K. Filsinger, B. Balke, G. H. Fecher, C. A. Jenkins, F. Casper, J. Kübler, G.-D. Liu, L. Gao, S. S. P. Parkin, and C. Felser, Adv. Mater. **24**, 6283 (2012).
[2] L. Wollmann, G. H. Fecher, S. Chadov, and C. Felser, J. Phys. D **48**, 164004 (2015).
[3] S. Chadov, S. W. D’Souza, L. Wollmann, J. Kiss, G. H. Fecher, and C. Felser, Phys. Rev. B **91**, 094203 (2015).
[4] B. Balke, G. H. Fecher, J. Kübler, and C. Felser, Appl. Phys. Lett. **90**, 152504 (2007).
[5] J. Winterlik, B. Balke, G. H. Fecher, C. Felser, M. C. M. Alves, F. Bernardi, and J. Morais, Phys. Rev. B **77**, 054406 (2008).
[6] D. Zhang, B. Yan, S.-C. Wu, J. Kübler, G. Kreiner, S. S. P. Parkin, and C. Felser, J. Phys. Condens. Matter **25**, 206006 (2013).
[7] H. Kurt, K. Rode, M. Venkatesan, P. Stamenov, and J. M. D. Coey, Phys. Rev. B **83**, 020405 (2011).
[8] S. S. P. Parkin, M. Hayashi, and L. Thomas, Science **320**, 190 (2008).
[9] S. Paul and S. Ghosh, J. Appl. Phys. **110**, 063523 (2011).
[10] S. Paul, S. Ghosh, and B. Sanyal, J. Phys. Condens. Matter **26**, 196004 (2014).
[11] V. Chernenko, E. Cesari, V. Kokorin, and I. Vitenko, Scr. Mater. **33**, 1239 (1995).
[12] K. Ullakko, J. K. Huang, C. Kantner, R. C. O’Handley, and V. V. Kokorin, Appl. Phys. Lett. **69**, 1966 (1996).
[13] V. Alijani, J. Winterlik, G. H. Fecher, and C. Felser, Appl. Phys. Lett. **99**, 222510 (2011).
[14] M. Meinert, J.-M. Schmalhorst, C. Klewe, G. Reiss, E. Arenholz, T. Böhnert, and K. Nielsch, Phys. Rev. B **84**, 132405 (2011).
[15] S. Ouardi, T. Kubota, G. H. Fecher, R. Stinshoff, S. Mizukami, T. Miyazaki, E. Ikenaga, and C. Felser, Appl. Phys. Lett. **101**, 242406 (2012).
[16] T. Kubota, S. Ouardi, S. Mizukami, G. H. Fecher, C. Felser, Y. Ando, and T. Miyazaki, J. Appl. Phys. **113**, 17C723 (2013).
[17] L. Wollmann, S. Chadov, J. Kübler, and C. Felser, Phys. Rev. B **90**, 214420 (2014).
[18] T. Gasi, A. K. Nayak, J. Winterlik, V. Ksenofontov, P. Adler, M. Nicklas, and C. Felser, Appl. Phys. Lett. **102**, 202402 (2013).
[19] T. Hori, M. Akimitsu, H. Miki, K. Ohoyoama, and Y. Yamaguchi, Appl. Phys. A **74**, s737 (2002).
[20] G. Kreiner, A. Kalache, S. Hausdorf, V. Alijani, J.-F. Qian, G. Shan, U. Burkhardt, S. Ouardi, and C. Felser, Z. Anorg. Allg. Chem. **640**, 738 (2014).
[21] A. K. Nayak, M. Nicklas, S. Chadov, C. Shekhar, Y. Skourski, J. Winterlik, and C. Felser, Phys. Rev. Lett. **110**, 127204 (2013).
[22] A. K. Nayak, M. Nicklas, S. Chadov, P. Khuntia, C. Shekhar, A. Kalache, M. Baenitz, Y. Skourski, V. K. Guduru, A. Puri, U. Zeitler, J. M. D. Coey, and C. Felser, Nat. Mater. **14**, 679 (2015).
[23] A. K. Nayak, C. Shekhar, J. Winterlik, A. Gupta, and C. Felser, Appl. Phys. Lett. **100**, 152404 (2012).
[24] F. Heusler, Verh. Dtsch. Phys. Ges. **5**(12), 219 (1903).
[25] J. C. Suits, Phys. Rev. B **14**, 4131 (1976).
[26] P. Blaha, K. Schwarz, G. K. H. Madsen, D. Kvasnicka, and J. Luitz, *WIEN2k: An Augmented Plane Wave + Local Orbitals Program for Calculating Crystal Properties* (Technische Universitat Wien, Vienna, 2001).
[27] J. P. Perdew, K. Burke, and M. Ernzerhof, Phys. Rev. Lett. **77**, 3865 (1996).
[28] F. Birch, Phys. Rev. **71**, 809 (1947).
[29] F. D. Murnaghan, Proc. Natl. Acad. Sci. U.S.A. **30**, 244 (1944).
[30] H. Ebert, D. Ködderitzsch, and J. Minár, Rep. Prog. Phys. **74**, 096501 (2011).
[31] P. Lloyd and P. V. Smith, Adv. Phys. **21**, 69 (1972).
[32] A. I. Liechtenstein, M. I. Katsnelson, P. V. Antropov, and A. V. Gubanov, J. Magn. Magn. Mater. **67**, 65 (1987).
[33] M. Meinert, J.-M. Schmalhorst, and G. Reiss, J. Phys. Condens. Matter **23**, 116005 (2011).
[34] G. Fritsch, V. V. Kokorin, V. A. Chernenko, A. Kempf, and I. K. Zasimchuk, Phase Transitions **57**, 233 (1996).
[35] V. A. Chernenko, C. Seguí, E. Cesari, J. Pons, and V. V. Kokorin, Phys. Rev. B **57**, 2659 (1998).
[36] A. Zheludev, S. M. Shapiro, P. Wochner, A. Schwartz, M. Wall, and L. E. Tanner, Phys. Rev. B **51**, 11310 (1995).
[37] U. Stuhr, P. Vorderwisch, V. V. Kokorin, and P.-A. Lindgård, Phys. Rev. B **56**, 14360 (1997).
[38] A. T. Zayak, P. Entel, J. Enkovaara, A. Ayuela, and R. M. Nieminen, Phys. Rev. B **68**, 132402 (2003).
[39] A. Chakrabarti, M. Siewert, T. Roy, K. Mondal, A. Banerjee, M. E. Gruner, and P. Entel, Phys. Rev. B **88**, 174116 (2013).
[40] S. Paul, B. Sanyal, and S. Ghosh, J. Phys. Condens. Matter **27**, 035401 (2015).

[41] P. J. Brown, T. Kanomata, K. U. Neumann, B. Ouladdiaf, A. Sheikh, and K. R. A. Ziebeck, J. Phys. Condens. Matter **22**, 506001 (2010).
[42] K. Endo, T. Kanomata, H. Nishihara, and K. R. A. Ziebeck, J. Alloys Compd. **510**, 1 (2012).
[43] M. Meinert, J.-M. Schmalhorst, and G. Reiss, J. Phys. Condens. Matter **23**, 036001 (2011).
[44] K. Ramesh Kumar, N. Harish Kumar, G. Markandeyulu, J. Arout Chelvane, V. Neu, and P. D. Babu, J. Magn. Magn. Mater. **320**, 2737 (2008).
[45] K. H. J. Buschow and P. G. van Engen, J. Magn. Magn. Mater. **25**, 90 (1981).
[46] H. Luo, Z. Zhu, G. Liu, S. Xu, G. Wu, H. Liu, J. Qu, and Y. Li, J. Magn. Magn. Mater. **320**, 421 (2008).
[47] G. D. Liu, X. F. Dai, H. Y. Liu, J. L. Chen, Y. X. Li, G. Xiao, and G. H. Wu, Phys. Rev. B **77**, 014424 (2008).
[48] G. D. Liu, J. L. Chen, Z. H. Liu, X. F. Dai, G. H. Wu, B. Zhang, and X. X. Zhang, Appl. Phys. Lett. **87**, 262504 (2005).
[49] O. Meshcheriakova, S. Chadov, A. K. Nayak, U. K. Rössler, J. Kübler, G. André, A. A. Tsirlin, J. Kiss, S. Hausdorf, A. Kalache, W. Schnelle, M. Nicklas, and C. Felser, Phys. Rev. Lett. **113**, 087203 (2014).
[50] H. Kurt, N. Baadji, K. Rode, M. Venkatesan, P. S. Stamenov, S. Sanvito, and J. M. D. Coey, Appl. Phys. Lett. **101**, 132410 (2012).
[51] H. Z. Luo, H. W. Zhang, Z. Y. Zhu, L. Ma, S. F. Xu, G. H. Wu, X. X. Zhu, C. B. Jiang, and H. B. Xu, J. Appl. Phys. **103**, 083908 (2008).
[52] A. T. Zayak, P. Entel, K. M. Rabe, W. A. Adeagbo, and M. Acet, Phys. Rev. B **72**, 054113 (2005).
[53] P. Entel, V. D. Buchelnikov, V. Khovailo, A. T. Zayak, W. A. Adeagbo, M. E. Gruner, H. C. Herper, E. F. Wassermann, and V, J. Phys. D **39**, 865 (2006).
[54] S. R. Barman, S. Banik, A. Shukla, C. Kamal, and A. Chakrabarti, Europhys. Lett. **80**, 57002 (2007).
[55] J. Kübler, A. R. Williams, and C. B. Sommers, Phys. Rev. B **28**, 1745 (1983).
[56] R. A. de Groot, F. M. Mueller, P. G. van Engen, and K. H. J. Buschow, Phys. Rev. Lett. **50**, 2024 (1983).
[57] H. Kurt, K. Rode, P. Stamenov, M. Venkatesan, Y.-C. Lau, E. Fonda, and J. M. D. Coey, Phys. Rev. Lett. **112**, 027201 (2014).
[58] D. Haskel, J. C. Lang, Z. Islam, A. Cady, G. Srajer, M. van Veenendaal, and P. C. Canfield, Phys. Rev. Lett. **95**, 217207 (2005).
[59] W. B. Yelon and J. F. Herbst, J. Appl. Phys. **59**, 93 (1986).
[60] J. Chaboy, L. M. García, F. Bartolomé, A. Marcelli, G. Cibin, H. Maruyama, S. Pizzini, A. Rogalev, J. B. Goedkoop, and J. Goulon, Phys. Rev. B **57**, 8424 (1998).